On the stability of Euler's elastica with natural curvature: Out-of-plane bifurcation with twisting

Lu Lu[a], Sophie Leanza[a], Ruike Renee Zhao[a], John W. Hutchinson[b*]

[a] Department of Mechanical Engineering, Stanford University, Stanford, CA 94305, USA
[b] School of Engineering and Applied Sciences, Harvard University, Cambridge, MA 02138, USA

*Corresponding author. Email: jhutchin@fas.harvard.edu (J.W. Hutchinson)

Abstract

Elastic rods can exhibit distinct buckling behavior in the presence of natural curvature due to the induced prestress. Recent work has shown that prestressed, clamped rods can undergo a secondary bifurcation from in-plane Euler buckling and subsequently exhibit twisting or snapping under axial compression. In this work, a bifurcation analysis for the secondary out-of-plane bifurcation of Euler's elastica is performed based on Kirchhoff's three-dimensional theory of inextensional rods. The critical end-shortening, critical load, and associated eigenmode at the onset of bifurcation are determined, and the role of natural curvature in the out-of-plane bifurcation from the Euler solution is systematically examined. It is found that the effect of natural curvature depends on the bending direction of Euler buckling. When the Euler buckling direction is consistent with the rod's naturally curved direction, the critical end-shortening decreases as the natural curvature increases, and vice versa. The imperfection sensitivity of the out-of-plane bifurcation is further investigated. The results reveal that the primary role of in-plane imperfections is to select the in-plane Euler buckling direction, which in turn has a major effect in the presence of substantial natural curvature. By contrast, the primary role of out-of-plane imperfections is to trigger the out-of-plane bifurcation and induce three-dimensional twisting or snapping.

Keywords: The elastica; Euler buckling; Out-of-plane bifurcation; Natural curvature; Imperfection.

1. Introduction

Euler buckling is one of the most fundamental instability phenomena in slender structures, which was initially solved by Euler in 1744, and the solution is now known as elastica theory [1]. Beyond its classical role in solid mechanics, Euler's elastica has recently emerged as an effective mechanism for designing reconfigurable and functional systems [2]. By harnessing its buckling-induced large deformation and instability-guided shape transformation, diverse applications have been explored, such as magnetic soft continuum robots for untethered navigation [3-5], flexible electronics with programmable shape morphing [6, 7], and mechanical metamaterials with programmable properties [8, 9]. In recent years, renewed interest has also been devoted to Euler buckling, or Euler's elastica, in a variety of material and structural systems, including nonlinear Euler buckling in hyperelastic materials [10, 11], Euler buckling on curved surfaces [12], and snap-through buckling in curved elastica [13-16].

In particular, our recent interest has focused on the buckling behavior of Euler's elastica in the presence of natural curvature [17-19]. In this case, a naturally curved slender rod is first straightened and then fixed at both ends, as illustrated in Fig. 1(a). Depending on the natural curvature as well as the bending and torsional stiffnesses, the rod can lose stability either through in-plane Euler buckling or through three-dimensional (3D) buckling involving bending and twisting [18]. For elastic rods with natural curvature that exhibit in-plane Euler buckling, our recent work [19] further demonstrated that a secondary out-of-plane bifurcation with twisting, followed by snapping, can occur when the end-shortening is sufficiently large. An experimental demonstration is shown in Fig. 1(b) and (c) as well as in Video 1 in the Supplementary Material (see Appendix A for experimental details). The rod has a rectangular cross-section with height-to-thickness ratio $h/t = 4$ and dimensionless natural curvature $\kappa_n L = 4\pi$, where L is the rod length. It initially undergoes in-plane Euler buckling (Fig. 1(b)). When the end-shortening reaches a critical value of $\Delta/L = 0.6$, out-of-plane twisting bifurcation occurs with subsequent snapping (Fig. 1(c)). Such out-of-plane twisting bifurcation behavior has also been observed previously in elastic rods without natural curvature [20-23]. Prior studies showed that, for naturally straight clamped rods, the critical end-shortening at twisting bifurcation increases with the torsional-to-bending stiffness ratio (positively correlated with h/t for isotropic materials), and the post-bifurcation behavior is typically dominated by twisting only without snapping [21-23]. For example, as shown in Fig. A1

in the Appendix and Video 1 in the Supplementary Material, twisting bifurcation occurs at a large end-shortening of $\Delta/L = 0.87$ for a rod with a large $h/t = 4$ but without natural curvature, where self-contact has already taken place. This is in sharp contrast to our experimental observations in Fig. 1, where the rod with natural curvature undergoes twisting bifurcation at relatively small end-shortening without self-contact and then snaps, indicating that natural curvature can strongly influence both the onset of twisting bifurcation and the subsequent post-bifurcation behavior. However, a systematic understanding of how natural curvature influences the onset and mode of out-of-plane bifurcation in elastic rods remains lacking.

In our previous work [19], we examined the post-bifurcation behavior of elastic rods with natural curvature using a numerical Kirchhoff rod model to guide the design of a novel reconfigurable mechanical system, termed elastic rod origami, with programmable static and dynamic properties. Here, to understand the fundamental mechanics underlying this instability behavior, we investigate the secondary out-of-plane bifurcation of Euler's elastica with natural curvature through a rigorous bifurcation analysis within the framework of Kirchhoff's 3D theory of inextensional rods. The critical end-shortening, critical load, and associated eigenmode at the onset of out-of-plane bifurcation are determined. The roles of natural curvature, as well as symmetric in-plane and antisymmetric out-of-plane geometric imperfections, in the out-of-plane bifurcation are further explored. It will be demonstrated that the natural curvature can delay or advance the onset of out-of-plane bifurcation, depending significantly on the bending direction of Euler buckling. The primary role of in-plane geometric imperfection is to select the Euler buckling direction, whereas that of out-of-plane geometric imperfection is to trigger the out-of-plane bifurcation and induce 3D twisting or snapping. These effects become significant in the presence of substantial natural curvature.

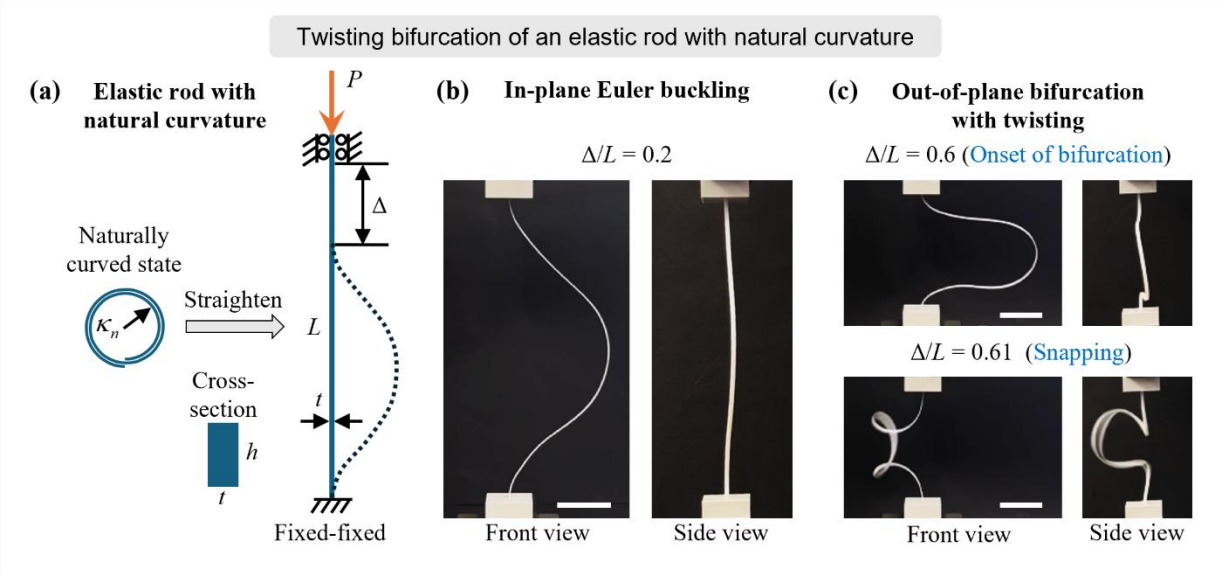

Fig. 1. Twisting bifurcation of an elastic rod with natural curvature under axial compression. (a) Schematic of an elastic rod with length L, rectangular cross-section height h, and thickness t. The naturally curved rod with curvature κ_n is first straightened and then fixed at both ends, with the top end allowed to displace axially under loading. In the experiment, an end-shortening Δ is prescribed, and the reaction force P is measured. (b, c) Experimental images of an elastic rod with $h/t = 4$ and $\kappa_n L = 4\pi$, corresponding to a 2-loop natural state, under axial compression. (b) At a small end-shortening, e.g., $\Delta/L = 0.2$, the rod exhibits in-plane Euler buckling. (c) As Δ/L reaches a critical value of 0.6, out-of-plane twisting bifurcation occurs, followed by snapping, as illustrated by the configuration at $\Delta/L = 0.61$. Scale bar: 3 cm.

The remainder of this paper is organized as follows. In Sections 2 and 3, we briefly review the buckling behavior of Euler's elastica with natural curvature and the classical Euler buckling solution, respectively. In Section 4, bifurcation analysis for the secondary out-of-plane bifurcation of Euler's elastica is performed, and the role of natural curvature in the out-of-plane bifurcation is examined in detail. In Section 5, we further investigate the imperfection sensitivity of the out-of-plane bifurcation and explore the roles of symmetric in-plane geometric imperfections and antisymmetric out-of-plane geometric imperfections. Finally, the main conclusions are summarized in Section 6.

2. Overview of buckling in Euler's elastica with natural curvature

We begin by briefly reviewing the buckling behavior of Euler's elastica with natural curvature. In our previous work [18], we analyzed the stability of the straight state of an axially compressed, clamped, inextensional Euler column, or rod, of length L with uniform natural

curvature κ_n. In the unstressed state, the rod lies in the $(\mathbf{i}_1, \mathbf{i}_2)$ plane with uniform natural curvature κ_n about $\mathbf{i}_3$, as illustrated in Fig. 2. It is straightened and clamped such that its centerline lies along the x_2-axis. The left end is fully clamped. A compressive force $-P\mathbf{i}_2$ acts at the right end, which is clamped so as to allow unrestricted motion parallel to the $\mathbf{i}_2$ axis. In the straightened state, the principal axes of the cross-section align with $\mathbf{i}_1$ and $\mathbf{i}_3$. The bending and twisting energy in the buckled rod is assumed to be governed by linear elasticity, with bending stiffnesses about these axes given by B_1 and B_3, and the torsional stiffness about the rod centerline by B_2.

$$\text{If } \left|\kappa_n L\right| > \kappa_n^{\max} L, \text{ where } \kappa_n^{\max} L = 2\pi\sqrt{\frac{B_1 B_2}{B_3{}^2}}, \tag{1}$$

the straight state is unstable when $P = 0$. Snap buckling occurs with out-of-plane bending and twisting. If, however, $\left|\kappa_n L\right| < \kappa_n^{\max} L$, stability of the straight state is lost in one of two ways. Assuming $B_1 \geq B_3$, and

$$\left|\kappa_n L\right| < \kappa_n^{*} L, \text{ where } \kappa_n^{*} L = 2\pi\sqrt{\left(\frac{B_1}{B_3} - 1\right)\frac{B_2}{B_3}}, \tag{2}$$

the straight state becomes unstable at the classical Euler load,

$$P_{Euler} = 4\pi^2 B_3 / L^2, \tag{3}$$

with bifurcation in the $(\mathbf{i}_1, \mathbf{i}_2)$ plane, which will be referred to as *in-plane* buckling. In the range of $\left|\kappa_n L\right| < \kappa_n^{*} L$, the natural curvature has no influence on the in-plane bifurcation from the straight state, nor, as will be seen shortly, on the subsequent in-plane buckling behavior until a secondary bifurcation occurs leading to *out-of-plane* buckling. The main thrust of this paper is to reveal the role of in-plane natural curvature in the range of $\left|\kappa_n L\right| < \kappa_n^{*} L$ on the secondary out-of-plane bifurcation of Euler rod which has buckled in the $(\mathbf{i}_1, \mathbf{i}_2)$ plane. The influence of small initial geometric imperfections will also be illustrated.

The second way in which stability of the straight state is lost occurs in the intermediate range of the natural curvature, $\kappa_n^* L < |\kappa_n L| < \kappa_n^{\max} L$. In this range, Leanza et al. [18] show that stability of the straight state is lost in the form of an out-of-plane bifurcation involving 3D bending and twisting. In this range, the natural curvature does influence the stability of the straight state such that the bifurcation load is

$$P_C = \frac{4\pi^2 B_1}{L^2} - \frac{(\kappa_n L)^2 B_3^{\,2}}{B_2 L^2}. \tag{4}$$

The initial post-bifurcation behavior in this range of natural curvature has also been determined by Leanza et al. [18], revealing that it can be stable or unstable depending on the bending and twisting stiffnesses, the natural curvature and whether the load or the end-shortening is prescribed.

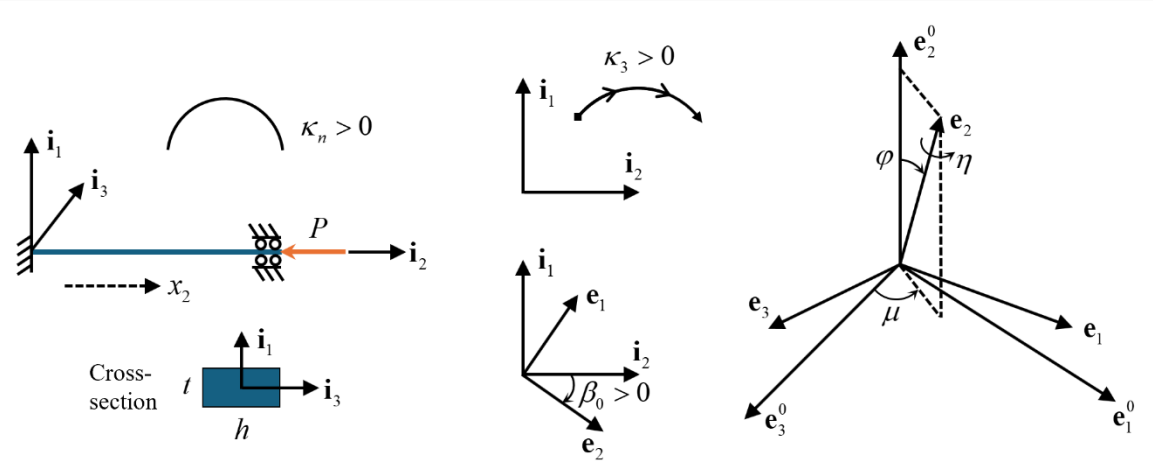

Fig. 2. Geometry, Euler angles, and sign conventions in the bifurcation analysis

As noted above, in this paper, we analyze the intriguing secondary out-of-plane bifurcation that occurs from the in-plane buckled state of the classical Euler column for natural curvatures in the range of $|\kappa_n L| < \kappa_n^* L$. In doing so, we will give a brief review of results in the literature for this problem for the case when there is no natural curvature. The out-of-plane bifurcation is anti-symmetric, with or without natural curvature, with one half of the rod deflecting and twisting out-of-the plane in one direction and the other half deflecting in the opposite direction. By contrast, the out-of-plane bifurcation in the range of $\kappa_n^* L < |\kappa_n L| < \kappa_n^{\max} L$ is symmetric, with the entire rod deflecting and twisting symmetrically with respect to the center of the rod.

3. The classical Euler solution for in-plane buckling

If the column is restricted to deflect in the $(\mathbf{i}_1, \mathbf{i}_2)$ plane, the energy of the column/loading system with a prescribed P is

$$\Psi = \frac{B_3}{L}\frac{1}{2}\int_0^1 \left\{ \left(\bar{\kappa}_3 - \bar{\kappa}_n\right)^2 - 2\bar{P}(1-\cos\beta_0) \right\} dx, \tag{5}$$

where the non-zero dimensionless curvatures are $\bar{\kappa}_3 = \kappa_3 L$ and $\bar{\kappa}_n = \kappa_n L$, and $\bar{P} = PL^2 / B_3$. The rotation of the unit tangent vector to the rod centerline, $\mathbf{e}_2$ about the x_3-axis, is $\beta_0(x)$ as seen in Fig. 2, and $x = s/L$, where s is the distance from the left end of the rod along the inextensional centerline. In addition, the dimensionless curvature about the x_3-axis measured from the straightened state is given by $\bar{\kappa}_3 = d\beta_0 / dx \equiv \beta_0'$, and the dimensionless displacement components measured from the straight state, ($\bar{u}_i = u_i / L$, $\bar{\mathbf{u}} = \bar{u}_i \mathbf{i}_i$), are related to β_0 by $\bar{u}_1' = -\sin\beta_0$, $\bar{u}_2' = \cos\beta_0$, and $\bar{u}_3 = 0$. It follows that the end-shortening, $\Delta = -u_2(L)$, through which P works, is given by

$$\Delta / L = \int_0^1 \left(1 - \cos\beta_0\right) dx. \tag{6}$$

Clamped conditions $u_1 = 0$ and $\beta_0 = 0$ at each end are required. Thus,

$$\bar{u}_1(x) = -\int_0^x \sin\beta_0 \, dx \quad \text{with the constraint} \quad \int_0^1 \sin\beta_0 \, dx = 0. \tag{7}$$

Stationarity of the system energy, i.e., Eq. (5), with respect to variations in $\beta_0(x)$ requires (recall that $\bar{\kappa}_n$ is independent of x)

$$\beta_0'' + \bar{P}\sin\beta_0 = 0, \quad \beta_0(0) = \beta_0(1) = 0, \tag{8}$$

subject to the constraint in Eq. (7). This is the classic Euler problem for a compressed rod clamped at its ends. Note that natural curvature has no influence on either the bifurcation buckling load or the post-buckling behavior. While the solution to this problem can be expressed in terms of elliptic

functions, here the solution has been obtained using numerical ODE solution methods of the same type required for solving the secondary out-of-plane bifurcation problem. Fig. 3 presents a plot of P/P_{Euler} versus Δ/L, where P_{Euler} is the classical Euler load at bifurcation load from the straight state shown in Eq. (3), and plots of $\beta_0(x)$ and the buckled shape at several values of end-shortening. These are plotted on the half-interval, $0 \le (x) \le 1/2$. The buckled shape is symmetric with respect to the center of the rod, such that $\beta_0(x)$ is anti-symmetric. The ODE (8) is solved on the half-interval with $\beta_0(1/2) = 0$.

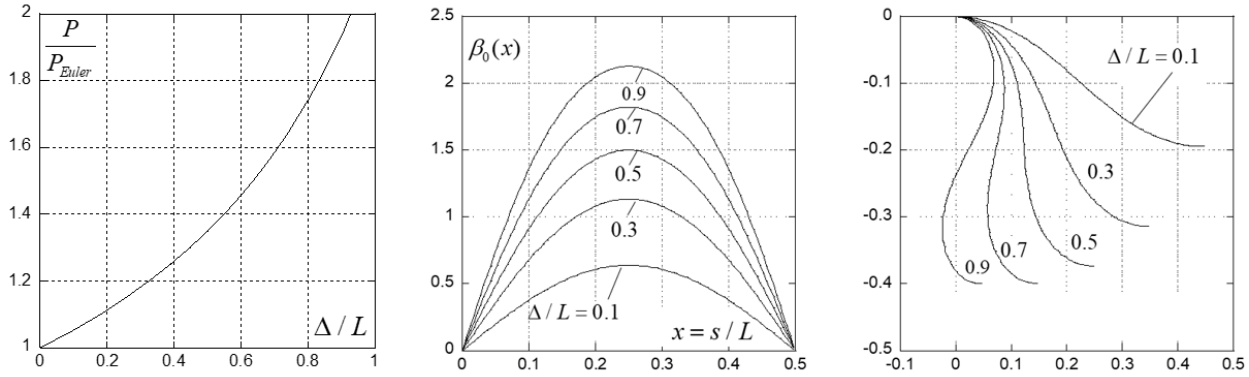

Fig. 3. In-plane buckling of the axially compressed Euler column. (Left) The post-buckling load end-shortening behavior. (Middle) The rotation of the centerline on the half-interval at various end-shortenings. (Right) The column shape on the half-interval for the same set of end-shortenings. The solutions depicted on the right will be referred to as *buckling down*. For the opposite sign of $\beta_0(x)$, the column *buckles up*. The load end-shortening curve is the same for buckling up or down, but the secondary out-of-plane bifurcation in the presence of natural curvature depends strongly on whether buckling is up or down!

4. Secondary out-of-plane bifurcation from the Euler solution

In the bifurcation analysis which follows, one can take either the compressive load P or the end-shortening Δ as the prescribed 'load' parameter. Both increase monotonically over the range of interest in Fig. 3. The classical Euler solution is symmetric about the column midpoint, and it does not have a limit point over the range plotted, nor are there any anti-symmetric in-plane bifurcations. We ask: When does the symmetric Euler solution, which lies in the $(\mathbf{i}_1, \mathbf{i}_2)$ plane become unstable bifurcating into either a symmetric or unsymmetric mode out-of-the $(\mathbf{i}_1, \mathbf{i}_2)$ plane with 3D bending and twisting? For this analysis, we employ 3D Kirchoff rod theory with three

Euler angles to measure the orientation of the triad of orthogonal unit vectors embedded in the rod on the out-of-plane solution branch to relative to the embedded triad in the deformed in-plane state at bifurcation. With a superscript '0' identifying the set of embedded unit vectors at bifurcation, one has

$$\mathbf{e}_1^0 = \cos\beta_0\mathbf{i}_1 + \sin\beta_0\mathbf{i}_2\,,\ \mathbf{e}_2^0 = -\sin\beta_0\mathbf{i}_1 + \cos\beta_0\mathbf{i}_2\,,\ \mathbf{e}_3^0 = \mathbf{i}_3. \tag{9}$$

With $\mathbf{e}_i(s)$ as the unit vectors of the triad on the out-of-plane branch of the solution, (η,φ,μ) is the set of angles defining the orientation of $\mathbf{e}_i(s)$, i = 1, 2, 3, relative to $\mathbf{e}_i^0(s)$, i = 1, 2, 3, as shown in Fig. 2. In particular, $\varphi(s)$ is the angle between the unit tangent vector $\mathbf{e}_2(s)$ and the unit tangent vector to the planar Euler solution at bifurcation $\mathbf{e}_2^0(s)$. The relations are

$$\begin{aligned}
\mathbf{e}_1 &= \left(\cos\eta\cos\mu - \cos\varphi\sin\eta\sin\mu\right)\mathbf{e}_1^0 + \sin\varphi\sin\eta\,\mathbf{e}_2^0 - \left(\cos\eta\sin\mu + \cos\varphi\sin\eta\cos\mu\right)\mathbf{i}_3,\\
\mathbf{e}_2 &= \sin\varphi\sin\mu\,\mathbf{e}_1^0 + \cos\varphi\,\mathbf{e}_2^0 + \sin\varphi\cos\mu\,\mathbf{i}_3,\\
\mathbf{e}_3 &= \left(\sin\eta\cos\mu + \cos\varphi\cos\eta\sin\mu\right)\mathbf{e}_1^0 - \sin\varphi\cos\eta\,\mathbf{e}_2^0 + \left(-\sin\eta\sin\mu + \cos\varphi\cos\eta\cos\mu\right)\mathbf{i}_3.
\end{aligned} \tag{10}$$

The curvature components on the out-of-plane solution expressed relative to the orthogonal embedded triad, $\mathbf{e}_i$, are

$$\begin{aligned}
\kappa_1 &= \cos\eta\left(\frac{d\varphi}{ds} - \frac{d\beta_0}{ds}\sin\mu\right) - \sin\eta\left(-\frac{d\mu}{ds}\sin\varphi + \frac{d\beta_0}{ds}\cos\varphi\cos\mu\right),\\
\kappa_2 &= \frac{d\eta}{ds} + \frac{d\mu}{ds}\cos\varphi + \frac{d\beta_0}{ds}\sin\varphi\cos\mu,\\
\kappa_3 &= \cos\eta\left(-\frac{d\mu}{ds}\sin\varphi + \frac{d\beta_0}{ds}\cos\varphi\cos\mu\right) + \sin\eta\left(\frac{d\varphi}{ds} - \frac{d\beta_0}{ds}\sin\mu\right).
\end{aligned} \tag{11}$$

These expressions reduce to those for a pre-bifurcation state that is a circular arc in the $(\mathbf{i}_1,\mathbf{i}_2)$ plane for which $d\beta_0/ds = 1/R$ [17]. Finally, the displacement components of the rod centerline from the *initial straight state* with $\mathbf{u} = u_1\mathbf{i}_1 + u_2\mathbf{i}_2 + u_3\mathbf{i}_3$ satisfy

$$\begin{aligned}
du_1/ds &= \cos\beta_0\sin\varphi\sin\mu - \sin\beta_0\cos\varphi,\\
du_2/ds &= \cos\beta_0\cos\varphi - 1 + \sin\beta_0\sin\varphi\sin\mu,\\
du_3/ds &= \sin\varphi\cos\mu.
\end{aligned} \tag{12}$$

Introduce non-dimensional quantities similar to those in Leanza et al. [18]:

$$x = s/L,\ (\,)' = d(\,)/dx,\ b_1 = B_1/B_3,\ b_2 = B_2/B_3,\ \bar{u} = u/L,\ \bar{\kappa} = L\kappa,\ \bar{P} = PL^2/B_3,\ \bar{\Psi} = \Psi L/B_3.$$

The dimensionless energy of the system on the secondary bifurcated branch with $\bar{P}$ prescribed is

$$\bar{\Psi} = \frac{1}{2}\int_0^1 \left\{ b_1\bar{\kappa}_1^{\,2} + b_2\bar{\kappa}_2^{\,2} + \left(\bar{\kappa}_3 - \bar{\kappa}_n\right)^2 - 2\bar{P}(1 - \cos\beta_0\cos\varphi - \sin\beta_0\sin\varphi\sin\mu) \right\} dx. \tag{13}$$

On the secondary bifurcation branch, all three of the new Euler angles (η, φ, μ) are zero at bifurcation. Expand $\bar{\Psi}$ to second order in (η, φ, μ). The zeroth-order terms are the energy at the bifurcated state. The contribution from the terms homogeneous of degree 1 vanishes because the bifurcation state is in equilibrium. The second-order contribution, which determines the stability of the in-plane Euler solution and the secondary bifurcation, is

$$\begin{aligned} \bar{\Psi}_2 = \frac{1}{2}\int_0^1 \Big\{ & b_1\left(\varphi' - \beta_0'(\eta + \mu)\right)^2 + b_2\left(\eta' + \mu' + \beta_0'\varphi\right)^2 \\ & - 2(\beta_0' - \bar{\kappa}_n)\left(\tfrac{1}{2}\beta_0'\left(\varphi^2 + (\mu + \eta)^2\right) + \varphi\mu' - \eta\varphi'\right) - \bar{P}\left(\cos\beta_0\,\varphi^2 - 2\sin\beta_0\,\varphi\mu\right) \Big\}\, dx. \end{aligned} \tag{14}$$

Boundary conditions associated with end clamping will be fully enforced, but note that the clamping requires $\mathbf{e}_i = \mathbf{e}_i^0 = \mathbf{i}_i, i = 1,3$ at the ends. By Eqs. (9) and (10), it follows that $\beta_0 = 0$, $\varphi = 0$, and $\psi = \eta + \mu = 0$ at the ends.

The quadratic bifurcation functional is reduced further by letting $\psi = \eta + \mu$. Then note the following, which follow from $\varphi(0) = \varphi(1) = 0$:

$$\bar{\kappa}_n\int_0^1 (\varphi\eta)'dx = 0, \quad \int_0^1 \beta_0'(\varphi\eta)'dx = -\int_0^1 \beta_0''\varphi\eta dx. \tag{15}$$

The only terms in $\bar{\Psi}_2$ involving η are

$$-2\int_0^1 \left(\beta_0'' + \bar{P}\sin\beta_0\right)\varphi\eta dx = 0, \tag{16}$$

and these vanish by Eq. (8). Thus, the bifurcation functional depends only on ψ and φ:

$$\bar{\Psi}_2 = \frac{1}{2}\int_0^1 \Big\{ b_1\left(\varphi' - \beta_0'\psi\right)^2 + b_2\left(\psi' + \beta_0'\varphi\right)^2 - 2(\beta_0' - \bar{\kappa}_n)\left(\tfrac{1}{2}\beta_0'\left(\varphi^2 + \psi^2\right) + \varphi\psi'\right) - \bar{P}\left(\cos\beta_0\,\varphi^2 - 2\sin\beta_0\,\varphi\psi\right)\Big\}\,dx. \tag{17}$$

The boundary conditions require ψ and φ to vanish at the ends of the rod, and φ is further constrained by the condition that u_3 vanishes at the ends requiring to this order, from Eq. (12), $\bar{u}_3' = \varphi$ such that $\int_0^1 \varphi dx = 0$. A slight variant on Eq. (17) that involves no constraint on φ is obtained by letting $\varphi = \bar{u}_3'$, as

$$\bar{\Psi}_2\left(\bar{u}_3, \psi, \bar{P}\right) = \frac{1}{2}\int_0^1 \Big\{ b_1\left(\bar{u}_3'' - \beta_0'\psi\right)^2 + b_2\left(\psi' + \beta_0'\bar{u}_3'\right)^2 - 2(\beta_0' - \bar{\kappa}_n)\left(\tfrac{1}{2}\beta_0'\left(\bar{u}_3'^2 + \psi^2\right) + \bar{u}_3'\psi'\right) - \bar{P}\left(\cos\beta_0\,\bar{u}_3'^2 - 2\sin\beta_0\,\bar{u}_3'\psi\right)\Big\}\,dx. \tag{18}$$

In this form, $\bar{\Psi}_2$ depends on $\bar{u}_3(x)$ and $\psi(x)$ with $\bar{u}_3$, $\bar{u}_3'$ and ψ required to vanish at the ends. It reduces to the corresponding functional derived by Leanza et al. [18] when the out-of-plane bifurcation occurs from the straight state with $\beta_0 = 0$.

Denote the lowest bifurcation load associated with the out-of-plane solution by $\bar{P}_C$. For loads below $\bar{P}_C$, stability to all sufficiently small disturbances requires $\bar{\Psi}_2 > 0$ for all admissible, nonzero combinations of $\bar{u}_3$ and ψ. The search for the lowest value of $\bar{P}$ such that there exists one or more nonzero ($\bar{u}_3, \psi$) with $\bar{\Psi}_2\left(\bar{u}_3, \psi, \bar{P}\right) = 0$ is an eigenvalue problem; $\bar{P} \equiv \bar{P}_C$ is the eigenvalue and ($\bar{u}_3, \psi$) is the eigenmode (or modes) which can be normalized as desired. Rendering $\bar{\Psi}_2$ stationary, $\delta\bar{\Psi}_2 = 0$, with respect to all admissible $(\bar{u}_3, \psi)$ generates the eigenvalue problem ODEs:

$$b_1\bar{u}_3'''' + \left[-b_2\beta_0'^2 + \left(\beta_0' - \bar{\kappa}_n\right)\beta_0' + \bar{P}\cos\beta_0\right]\bar{u}_3'' + \left[(2b_2 - 3)\beta_0' + \bar{\kappa}_n\right]\bar{P}\sin\beta_0\,\bar{u}_3' + \left[(-b_1 - b_2 + 1)\beta_0' - \bar{\kappa}_n\right]\psi'' + \left[2b_1 - b_2 - 2\right]\bar{P}\sin\beta_0\,\psi' + \left[b_1 - 1\right]\bar{P}\beta_0'\cos\beta_0\,\psi = 0, \tag{19}$$

$$b_2\psi'' + \left[(b_1 + b_2 - 1)\beta_0' + \bar{\kappa}_n\right]\bar{u}_3'' - b_2\bar{P}\sin\beta_0\,\bar{u}_3' - \left[(b_1 - 1)\beta_0' + \bar{\kappa}_n\right]\beta_0'\psi = 0, \tag{20}$$

with $\bar{u}_3$, $\bar{u}_3'$ and ψ vanishing at $x=0$ and $x=1$.

The in-plane buckled Euler column shape is symmetric about the rod mid-point, with the angle of the tangent vector to the centerline, $\beta_0(x)$, being anti-symmetric. The x dependence of each of coefficients in the two ODEs, which depend on $\beta_0(x)$, is either symmetric or anti-symmetric about $x=1/2$ such that the eigenmodes will be either symmetric or anti-symmetric about $x=1/2$. Over the entire range of parameters considered in this paper, we have found that the eigenmode associated with the lowest, or critical, eigenvalue, $\bar{P}_C$, is always anti-symmetric about $x=1/2$, i.e., $\bar{u}_3(x)$ and $\psi(x)$ are anti-symmetric about $x=1/2$. For such modes, the ODE can be solved on the half-interval, $0\le x\le 1/2$, with $\bar{u}_3=0$, $\bar{u}_3''=0$ and $\psi=0$ as boundary conditions at $x=1/2$. We have used the numerical ODE solver, BFPFD (IMSL, 2021), to obtain the critical eigenvalue and associated eigenmode. The eigenmode has been normalized such that the maximum value of $\bar{u}_3(x)$ on the half-interval is unity.

4.1. Out-of-plane of bifurcation from the Euler solution with no natural curvature

Results from the literature can be found for the problem of interest in the absence of natural curvature. A selection of these results has been used to validate our formulation and numerical method. Rods formed from isotropic elastic materials with Young's modulus E and Poisson's ratio ν with circular solid or concentric annular cross-sections have $b_1=B_1/B_3=1$ and $b_2=B_2/B_3=1/(1+\nu)$. The dependence of the dimensionless end-shortening at the point of out-of-plane bifurcation for these rods is presented as a function of ν in Fig. 4. The two numerical values recorded on the figure agree to three significant figures to those given in the literature [20-23]. The dependence on Poisson's ratio is not negligible. Note also that for these cases with no natural curvature, the out-of-plane bifurcation occurs at large in-plane buckling deflections. Again, we emphasize these results do not depend on the sign of the in-plane buckling deflection, i.e., on whether the rod buckles up or down. The corresponding values of P_C/P_{Euler} can be read off the plot in Fig. 3.

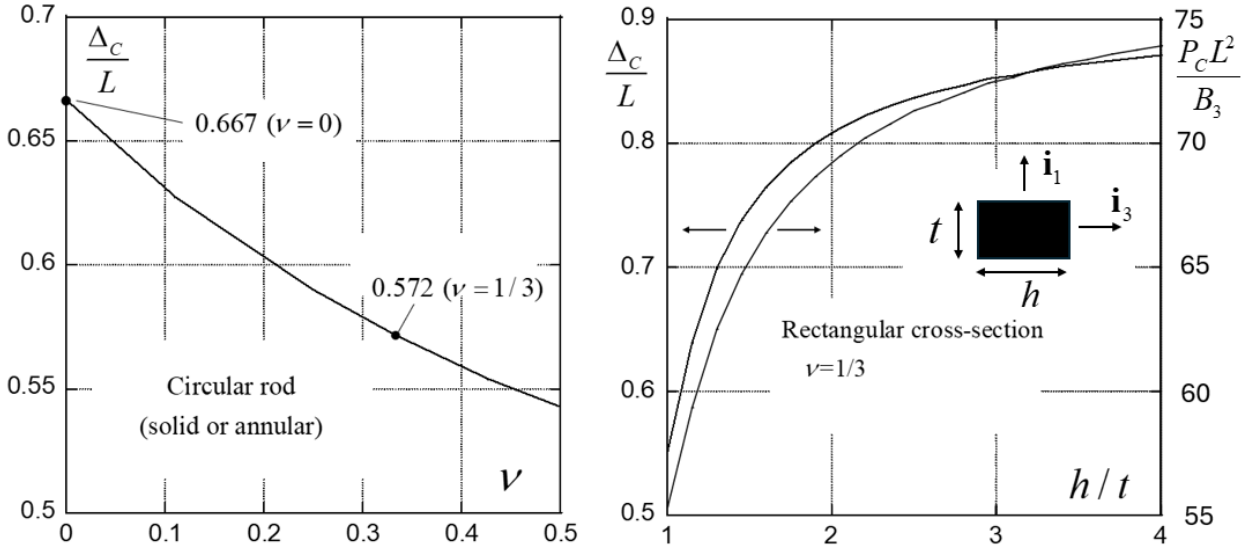

Fig. 4. Values of the end-shortening and axial compressive load at the state at which out-of-plane bifurcation occurs when there is no natural curvature. (Left) For rods with circular cross-sections, as dependent on Poisson's ratio. (Right) For rods with solid rectangular cross-sections with $\nu = 1/3$. The associated dimensionless compressive load is also plotted for the rectangular cross-sections.

The energy functional for the special case of rods with no natural curvature which have two equal bending stiffnesses which are also equal to the torsional stiffness, such as rods with circular cross-sections and $\nu = 0$, reduces to a simpler form. Several authors have referred to such rods as being 'isotropic'. The authors of these papers have been able to obtain analytical results for this special case not only for the secondary out-of-plane bifurcation point but also for the subsequent out-of-plane post-bifurcation behavior [20, 21, 23].

Stump and van der Heijden [22] have provided numerical results for out-of-plane bifurcation and post-bifurcation behavior for rods of rectangular cross-section with no natural curvature, and their numerical values for the bifurcation are in agreement with those on the right in Fig. 4 to the extent that can be inferred from their numerical plots. These pertain to rods with rectangular cross-sections made from isotopically elastic materials with $b_1 = B_1 / B_3 = (h/t)^2$. An accurate approximation for the torsional stiffness of a rod with a rectangular cross-section has been given by Sokolnikoff [24], which provides

$$b_2 = \frac{B_2}{B_3} = \frac{2}{1+\nu}\left(1 - \frac{192}{\pi^5}\frac{t}{h}\tanh\left(\frac{\pi}{2}\frac{h}{t}\right)\right). \tag{21}$$

Fig. 4 reveals that increasing h/t, which increases the out-of-plane bending stiffness relative to the in-plane bending stiffness, significantly delays out-of-plane bifurcation, as expected.

4.2. The role of natural curvature in out-of-plane bifurcation from the Euler solution

As emphasized earlier, this section analyzes the out-of-plane bifurcation in the range of natural curvatures, $|\kappa_n L| < \kappa_n^* L$, for which in-plane Euler buckling precedes out-of-plane buckling. Out-of-plane buckling initiates as a secondary bifurcation at compressive loads above P_{Euler}. The numerical analysis of the out-of-plane bifurcation reveals that the mode associated with the lowest eigenvalue, P_C (or Δ_C), is *anti-symmetric* with respect to the center of the rod, except possibly very near the ends of the range, $|\kappa_n L| \cong \kappa_n^* L$. That is, the out-of-plane deflection of the rod and the twist vanish at the center with equal and opposite values at $x = 1/2 + a$ and $x = 1/2 - a$. Example plots of the bifurcation mode will be shown later.

Rods made from an isotropic elastic material with circular or square cross-sections have identical in-plane and out-of-plane bending stiffnesses (i.e., $B_3 = B_1$) and, thus, by Eq. (2), $\kappa_n^* = 0$. Such rods lie outside our current range of interest. In the presence of natural curvature, their first bifurcation from the straight state occurs at loads below P_{Euler} in the form of a *symmetric* mode involving out-of-plane deflection and twist, as analyzed by Leanza et al. [18]. Rods with rectangular cross-section having greater out-of-plane relative to in-plane stiffness, i.e., $h/t > 1$ with $b_1 = (h/t)^2 > 1$, have $\kappa_n^* > 0$, and these rods will be used to illustrate the role of natural curvature on out-of-plane bifurcation from the Euler buckled state.

Fig. 5 presents the dimensionless end-shortening, Δ_C / L, at the out-of-plane bifurcation point as a function of the dimensionless natural curvature $\kappa_n L$ for rods with rectangular cross-section ($h/t = 2, 3, 4$) and $\nu = 1/3$. The large effect of natural curvature is evident. The figure also highlights the importance of the sign of the in-plane Euler solution relative to the sign of the natural curvature. In Fig. 5(a), the in-plane Euler deflection is downward, and in Fig. 5(b) it is upward. Results over the entire range of $|\kappa_n L| < \kappa_n^* L$ have not been presented, but we believe the range covered will be of the most interest. At the end of the range where Δ_C / L is the largest, we have

terminated the curves at $\Delta_C / L \cong 0.9$ which is roughly the point at which the Euler solution makes self-contact (c.f., Fig. 3). In addition, results have not been presented at the other end of the range where Δ_C / L is the smallest for reasons discussed shortly.

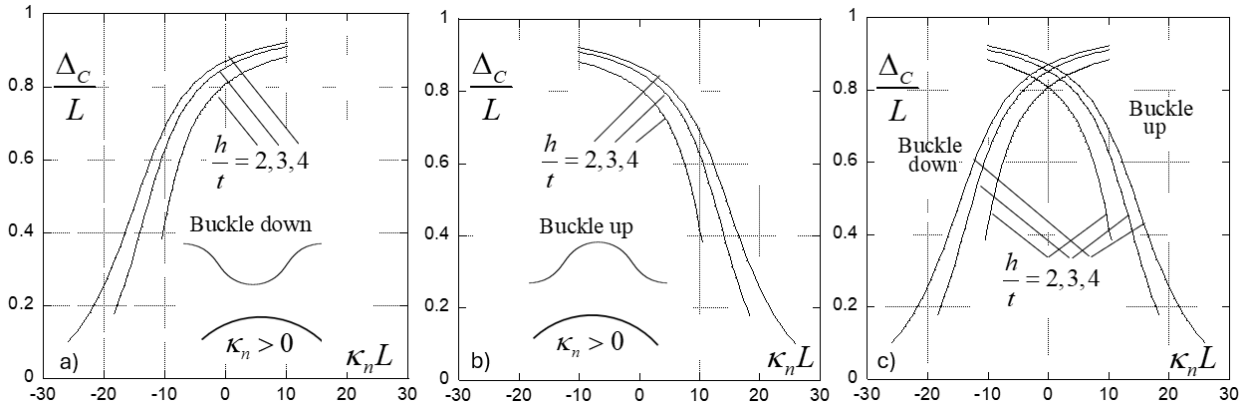

Fig. 5. The effect of uniform natural curvature on the out-of-plane bifurcation from the classical Euler solution for rods with rectangular cross-sections ($h/t = 2,3,4$) in the range of $|\kappa_n L| < \kappa_n^* L$. As discussed in the text, the effect depends strongly on whether the in-plane pre-bifurcation Euler buckling is down (a) or up (b). A composite of the results for both up and down pre-buckling deflections is given in (c). For these results: $\nu = 1/3$, with $\kappa_n^* L = 11.05$ for $h/t = 2$, $\kappa_n^* L = 19.4$ for $h/t = 3$, and $\kappa_n^* L = 27.4$ for $h/t = 4$. The associated values of the dimensionless bifurcation load $P_C L^2 / B_3$ can be determined from Fig. 4.

Table 1. Critical end-shortening (Δ_C/L) at the out-of-plane bifurcation of elastic rods with rectangular cross-section and Poisson's ratio 1/3 for different values of dimensionless natural curvatures. The results correspond to Euler buckling being down, as illustrated in Fig. 5(a). For $h/t = 2$ and 3, $\kappa_n L = \pm 20$ is outside the range of natural curvature for exhibiting in-plane pre-bifurcation Euler buckling.

	$h/t = 2$		$h/t = 3$		$h/t = 4$		
$\kappa_n L$	Bifurcation analysis	Numerical results	Bifurcation analysis	Numerical results	Bifurcation analysis	Numerical results	Experiment
−20	---	---	---	---	0.256	0.2557	0.41
−10	0.426	0.4244	0.628	0.6273	0.690	0.6900	0.68
0	0.808	0.8073	0.852	0.8522	0.871	0.8702	0.87
10	0.882	0.8818	0.910	0.9102	0.921	0.9209	0.84
20	---	---	---	---	0.943	0.9430	0.83

The steep reduction in the end-shortening causing out-of-plane bifurcation, Δ_C / L, occurs when κ_n is negative if Euler buckling is down and vice versa. The plots for buckling up and

buckling down are mirror images of one another, consistent with the up/down symmetry when the sign of the natural curvature is switched. Fig. 5(c) combines the results in Fig. 5(a) and (b), including both up and down Euler buckling. Unless the direction of Euler buckling, up or down, is 'forced' by external means, the direction of the Euler buckling will almost certainly be determined by imperfections in the rod or in the loading system. Further, the fact that the natural curvature has such a strong influence on the end-shortening for out-of-plane bifurcation will likely result in the rod being most sensitive to the imperfections that push Euler buckling in the direction of the smaller, rather than the larger, critical end-shortening.

The theoretical predictions in the presence of natural curvature from the bifurcation analysis are compared with the numerical results obtained from an independent Kirchhoff rod model presented in our previous work [19]. The results are summarized in Table 1, with the Euler buckling direction downward, corresponding to the case shown in Fig. 5(a). Excellent agreement is observed between the current theoretical predictions and the previous numerical results. Experimental results for elastic rods with $h/t = 4$ are also provided, showing reasonable agreement. In particular, for $\kappa_n L$ = 0, 10, and 20, out-of-plane bifurcation occurs at a very large end-shortening, where self-contact takes place. To avoid self-contact and facilitate the onset of bifurcation in the experiments, a small out-of-plane end offset is applied at the loading end.

As noted above, results for values of natural curvature approaching $\pm\kappa_n^*$ have not been presented. The mathematical behavior for natural curvatures in the vicinity of $\pm\kappa_n^*$ is almost certainly complicated. Bifurcation when $\kappa_n = \kappa_n^*$ and $\kappa_n = -\kappa_n^*$ has been analyzed by Leanza et al. [18], revealing that: (1) at out-of-plane bifurcation, the rod is straight with $P_C = P_{Euler}$, and (2) the bifurcation mode is symmetric with respect to the rod center. Results from the present analysis as $\kappa_n \to \pm\kappa_n^*$ from inside the range $|\kappa_n| < \kappa_n^*$ suggests that the out-of-plane bifurcation mode is anti-symmetric with $P_C > P_{Euler}$. We have not sorted out the mathematical details of the behavior in the 'tails' of the range. The details will almost certainly involve interaction between the symmetric and anti-symmetric modes.

Representative examples of the anti-symmetric eigenmode shapes for out-of-plane bifurcations are plotted in Fig. 6. Neither the magnitude nor the sign of the mode is determined

by the bifurcation analysis. In the figure, modes have been normalized such that the maximum value of u_3 / L is unity.

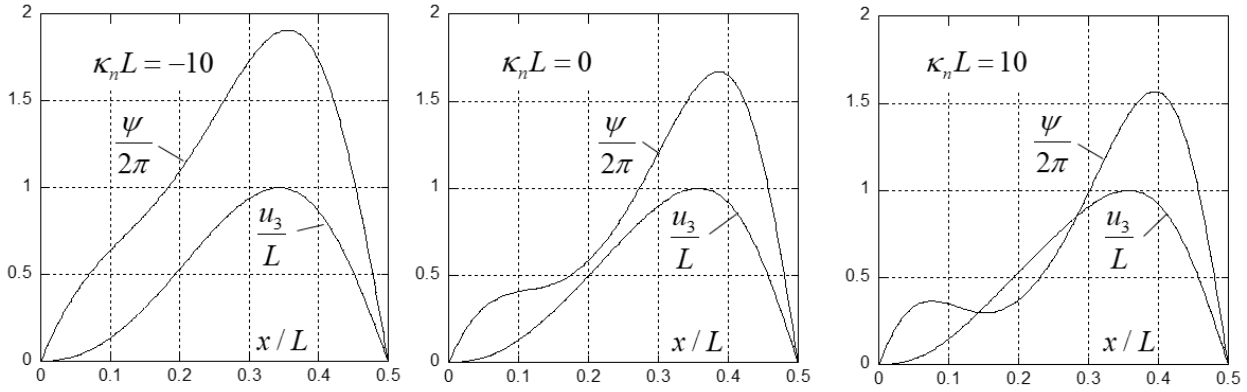

Fig. 6. Out-of-plane bifurcation eigenmodes for rods with rectangular cross-section with $h/t = 2$, $\nu = 1/3$, and three natural curvatures, $\kappa_n L = -10, 0, 10$. The modes have been normalized such that $(u_3 / L)_{\max} = 1$.

5. Imperfection sensitivity of out-of-plane bifurcation in elastic rods

The imperfection sensitivity of the out-of-plane bifurcation in elastic rods with natural curvature is further investigated. Two types of geometric imperfections are considered: symmetric in-plane geometric imperfections and anti-symmetric out-of-plane geometric imperfections.

5.1. The role of in-plane geometric imperfections

The in-plane Euler solution is symmetric with respect to the center of the buckled rod. Imperfections in the form of in-plane geometric non-uniformities of the rod will be amplified the most by the compressive load and have the most severe effect if they are also symmetric, and we restrict attention to symmetric in-plane imperfections. Superimposed on the uniform natural curvature about the x_3-axis, κ_n, is an imperfection in the form of a small nonuniform natural curvature given by

$$\kappa_n^I = d\beta_I / ds = \bar{\xi}(2\pi^2 t / L^2)\cos(2\pi s / L) \text{ with } \beta_I = \bar{\xi}(\pi t / L)\sin(2\pi s / L), \tag{22}$$

where t is the in-plane thickness of the rectangular cross-section of the rod and $\bar{\xi}$ is the dimensionless imperfection amplitude. With a moment, $M_3 = -B_3\kappa_n$, applied to each end of the

rod, the rod becomes nearly straight, apart from the effect of the imperfection, and the slopes at the ends of the rod are zero. The rod can be inserted into the compression rig and clamped with an initial slope distribution given by $\beta_I = \bar{\xi}(\pi t / L)\sin(2\pi s / L)$ (when $P = 0$). We will limit the imperfection amplitude, $\bar{\xi}$, to be small in the sense that $\left|\beta^I\right| << 1$, such that $du_1 / ds \cong -\beta_I$ when $P = 0$. Thus, the in-plane deflection of the rod in the unloaded state ($P = 0$) is

$$u_1^I \cong -\bar{\xi}\,\frac{t}{2}\big(1-\cos(2\pi s / L)\big). \tag{23}$$

An amplitude with $\left|\bar{\xi}\right| = 1$ corresponds to an imperfection deflection magnitude at the center of the rod of one thickness with $\bar{\xi} > 0$ corresponding to a downward deflection and vice versa. The imperfection modifies the ODE governing the in-plane Euler problem, Eq. (8), such that with $\beta_0(x)$ continuing as the angle of rotation measured from the direction $\mathbf{i}_2$, as in Fig. 2, the exact equations governing the in-plane behavior are

$$\begin{aligned} &\beta_0'' + \bar{P}\sin\left(\beta_0\right) = \beta_I'', \quad \beta_0(0) = \beta_0(1/2) = 0, \\ &\Delta / L = 2\int_0^{1/2}\left(1-\cos\beta_0\right)dx, \end{aligned} \tag{24}$$

where, as earlier, $x = s / L$, and anti-symmetry of $\beta_0(x)$ is assumed.

The introduction of an imperfection usually results in the maximum load occurring at a limit point, however, not in the case of an in-plane imperfection. For the imperfections considered in this section, the secondary buckling load still occurs as an out-of-plane bifurcation. The functional $\bar{\Psi}_2$ in Eq. (17) still governs this bifurcation, but one term must be modified, i.e., in the third term, $(\beta_0' - \bar{\kappa}_n)$ must be replaced by $(\beta_0' - \bar{\kappa}_n - \bar{\kappa}_n^I)$. In turn, this modification requires that $-(\bar{\kappa}_n^I \beta_0' \bar{u}_3')' - (\bar{\kappa}_n^I \psi')'$ be added to the left-hand side of ODE (19) and that $-\bar{\kappa}_n^I \beta_0' \psi + (\bar{\kappa}_n^I \bar{u}_3')'$ be added to the left-hand side of ODE (20). It should be noted that the modified equations apply for any in-plane imperfection with β_I zero at the ends and curvature $\bar{\kappa}_n^I(x) = \beta_I'$ that is symmetric about the center of the rod. Additional modifications are required if the imperfection is not symmetric about the center. In particular, the rod will generally be subject to a uniform vertical force in addition to the applied horizontal force P, which must be included in the formulation.

Plots of the in-plane load/end-shortening and load/buckling amplitude behavior as dependent on small imperfections (Eqs. (22) and (23)) are presented for a representative example in Fig. 7. For a typical slender rod with $t/L \le 0.01$, the imperfection levels plotted are not unrealistic. It is important to recall that the natural curvature κ_n has no influence on the curves in Fig. 7.

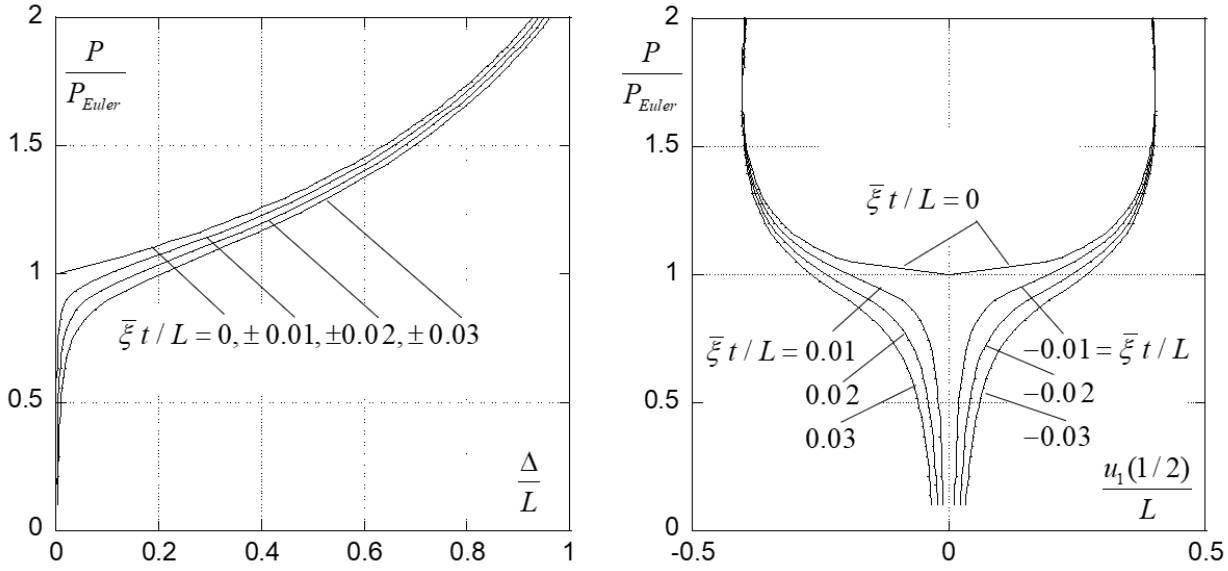

Fig. 7. The effect of the small geometric in-plane imperfection (Eqs. (22) and (23)) (Left) on the in-plane load/end-shortening behavior of the Euler rod, and (Right) on the load/buckling deflection at the center of the rod. These results assume that the load or end-shortening is applied monotonically from zero with no external agent acting to change the direction of buckling. For this example, the rod has a rectangular cross-section with $h/t = 4$ and $\nu = 1/3$. The uniform natural curvature κ_n has no influence on the in-plane behavior.

The effect of the imperfection seen in Fig. 7 is typical for the stable in-plane behavior of a compressed Euler rod in that it only produces modest alterations and does not give rise to a substantial loss of load-carrying capacity. In other words, the sensitivity to in-plane imperfections is modest. When the rod is subject to a monotonically increasing load or end-shortening from zero, the sign of the in-plane imperfection selects whether the buckling is down or up. For the sign conventions in this paper, $\bar{\xi} > 0$ causes buckling down and $\bar{\xi} < 0$ causes buckling up, as seen on the right in Fig. 7. We have not plotted other solution branches in Fig. 7 that lie above those for the perfect rod, $\bar{\xi} = 0$. For example, if rods with $\bar{\xi} < 0$ in Fig. 7 were forced by an external agent to buckle down, they would support slightly higher loads at the same end-shortening.

The strong influence of the uniform natural curvature κ_n on the out-of-plane bifurcation in the presence of an in-plane imperfection is illustrated in Fig. 8 for the same rod example discussed in Fig. 7. The curves apply for positive imperfections and buckling down in-plane behavior. These results have been computed with the modified eigenvalue equations. To a reasonable approximation, the critical end-shortening at out-of-plane bifurcation in the presence of the imperfection is nearly the same as for the perfect rod, with detailed values summarized in Table 2. Again, the conclusion to be drawn is that uniform natural curvature κ_n has a major effect on out-of-plane bifurcation, while the in-plane imperfections have a relatively modest effect on the bifurcation. The important role of the in-plane imperfection is to select whether the in-plane buckling is down or up which, in turn, has a major effect in the presence of substantial κ_n.

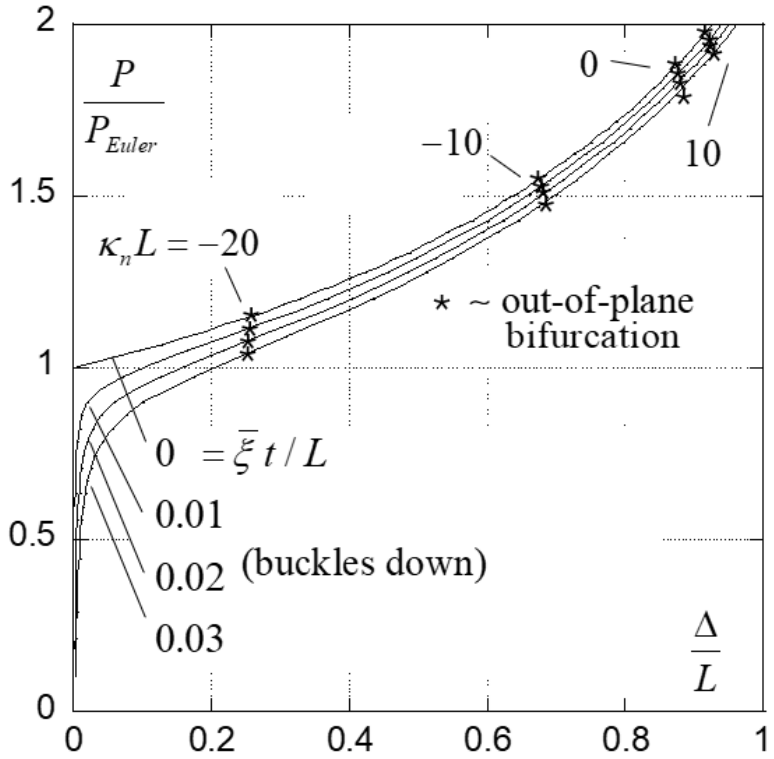

Fig. 8. The effect of uniform natural curvature κ_n combined with the in-plane geometric imperfection on the out-of-plane bifurcation. The rod has a rectangular cross-section with $h/t = 4$ and $\nu = 1/3$. Starting from the unloaded state, imperfections with $\bar{\xi} > 0$ cause the initial in-plane Euler buckling to be downward. Out-of-plane bifurcation results are shown for four values of natural curvature: $\kappa_n L = -20, -10, 0, 10$ ($\kappa_n^* L = 27.4$). Identical results are obtained for $\bar{\xi} < 0$ with upward in-plane buckling, but with the signs of the natural curvature switched.

Table 2. Critical end-shortening and the corresponding load at the out-of-plane bifurcation of elastic rods with in-plane geometric imperfection (h/t = 4 and ν = 1/3). The Euler buckling direction is down, corresponding to the case in Fig. 5(a).

	$\kappa_n L = -20$		$\kappa_n L = -10$		$\kappa_n L = 0$		$\kappa_n L = 10$	
$\bar{\xi} t / L$	Δ_C / L	P_C / P_{Euler}	Δ_C / L	P_C / P_{Euler}	Δ_C / L	P_C / P_{Euler}	Δ_C / L	P_C / P_{Euler}
0	0.256	1.150	0.691	1.571	0.870	1.872	0.921	1.982
0.01	0.254	1.114	0.692	1.547	0.873	1.857	0.924	1.960
0.02	0.252	1.078	0.693	1.522	0.877	1.831	0.926	1.938
0.03	0.249	1.041	0.695	1.498	0.879	1.810	0.928	1.916

5.2. The role of out-of-plane geometric imperfections

An out-of-plane geometric imperfection is introduced in the form of pre-twist, with the pre-twist angle varying linearly along the longitudinal direction of the rod, as

$$\gamma(s) = \gamma_m \left(\frac{2s}{L} - 1 \right), \quad s \in [0, L], \tag{25}$$

where γ_m is the imperfection amplitude. Such an imperfection is antisymmetric about the midpoint of the rod and is expected to trigger the secondary bifurcation, leading to out-of-plane deformation. Here, the effect of this antisymmetric geometric imperfection on the out-of-plane bifurcation behavior of elastic rods with natural curvature is studied using finite element simulations. In the simulations, the imperfection is created by applying a pair of twisting angles, i.e., γ_m and $-\gamma_m$, at the two ends of the rod. The resulting deformed configuration is then exported to release the strain, and the stress-free configuration serves as the initial configuration of the rod with natural curvature. More details of the finite element simulations are provided in Appendix B.

Figs. 9(a-c) and 10(a-c) illustrate the dimensionless load as a function of the dimensionless end-shortening for elastic rods with positive or negative natural curvature, under axial compression, for different pre-twist imperfection amplitudes. The rod has a rectangular cross-section with h/t = 4 and ν = 1/3. The Euler buckling direction is consistent with the rod's naturally curved direction, corresponding to the case shown in Fig. 5(b). For rods with different natural curvatures, the antisymmetric pre-twist geometric imperfection has little influence on the rod behavior before the secondary bifurcation. However, out-of-plane bifurcation is triggered when the end-shortening reaches a critical value, and the rod transitions to an equilibrium branch with a lower load, even for an imperfection amplitude as small as 0.01 rad (0.57 degrees). As the imperfection amplitude

increases from 0.01 to 0.1 rad, the critical end-shortening at bifurcation decreases slightly. This indicates that the primary role of the antisymmetric pre-twist geometric imperfection is to trigger the out-of-plane bifurcation, while having only a limited effect on the critical load or end-shortening at the onset of bifurcation.

In the absence of natural curvature, or when the magnitude of natural curvature is relatively small (e.g., $\kappa_n L = \pm\pi$), the rod undergoes significant twisting after bifurcation, as illustrated in Figs. 9(d-e) and 10(d-e) and observed experimentally in Fig. A1 in the Appendix. By contrast, when the rod has a relatively large positive natural curvature (e.g., $\kappa_n L = 3.18\pi$), it exhibits snapping after the onset of twisting bifurcation and transitions into a 2-loop overlapping circle as the end-shortening further increases (Fig. 9(f)). A more comprehensive parametric study based on the Kirchhoff rod model in our previous work [19] indicated that, for $h/t = 4$ and $\nu = 1/3$, the critical natural curvature separating twisting and snapping post-bifurcation behavior is approximately $\kappa_n L = 2.28\pi$. When the rod has a relatively large-magnitude negative natural curvature (e.g., $\kappa_n L = -3.18\pi$), the rod first undergoes twisting and then snapping after the onset of bifurcation, as shown in Fig. 10(f). However, such post-bifurcation behavior occurs at very large end-shortening, where self-contact takes place. These results further reveal that the post-bifurcation behavior also significantly depends on both the natural curvature and the Euler buckling direction. By appropriately controlling these two factors, the rod can exhibit different post-bifurcation behavior, including twisting, snapping, and twisting followed by snapping.

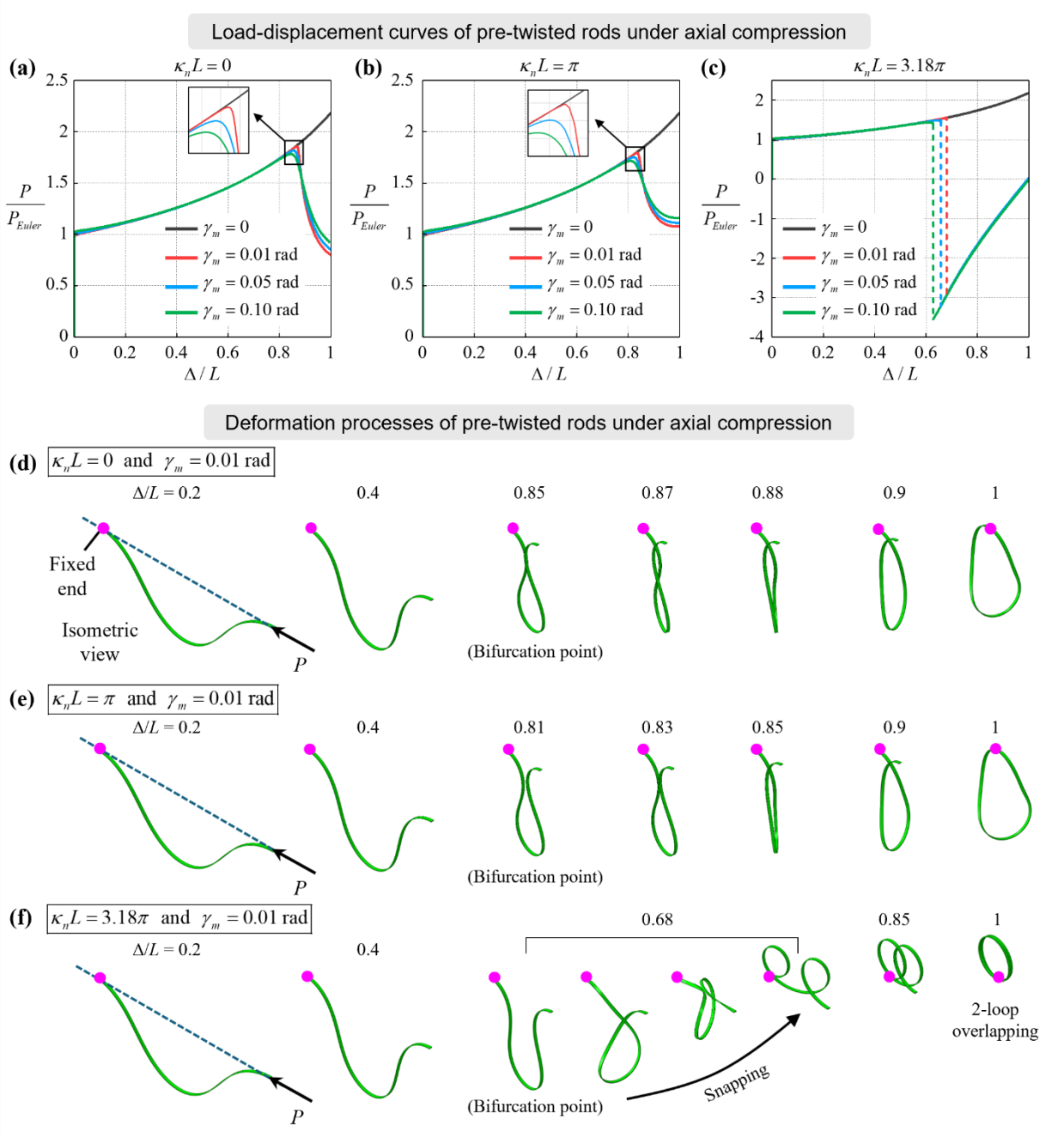

Fig. 9. Mechanical behavior of pre-twisted elastic rods with *positive* natural curvatures under axial compression, predicted by finite element simulations. (a-c) Dimensionless load P/P_{Euler} versus dimensionless end-shortening Δ/L for different pre-twisted angles γ_m: (a) $\kappa_n L = 0$; (b) $\kappa_n L = \pi$; (c) $\kappa_n L = 3.18\pi$. Here, $P_{Euler} = 7.6231$ N is the Euler buckling load predicted by finite element simulations, which is slightly smaller than the theoretical value 7.8271 N. The dashed lines in (c) correspond to the snapping process. (d-e) Deformation processes of elastic rods with $\gamma_m = 0.01$ rad: (d) $\kappa_n L = 0$; (e) $\kappa_n L = \pi$; (f) $\kappa_n L = 3.18\pi$. In all cases, $h/t = 4$ and $\nu = 1/3$. The dot represents the fixed end.

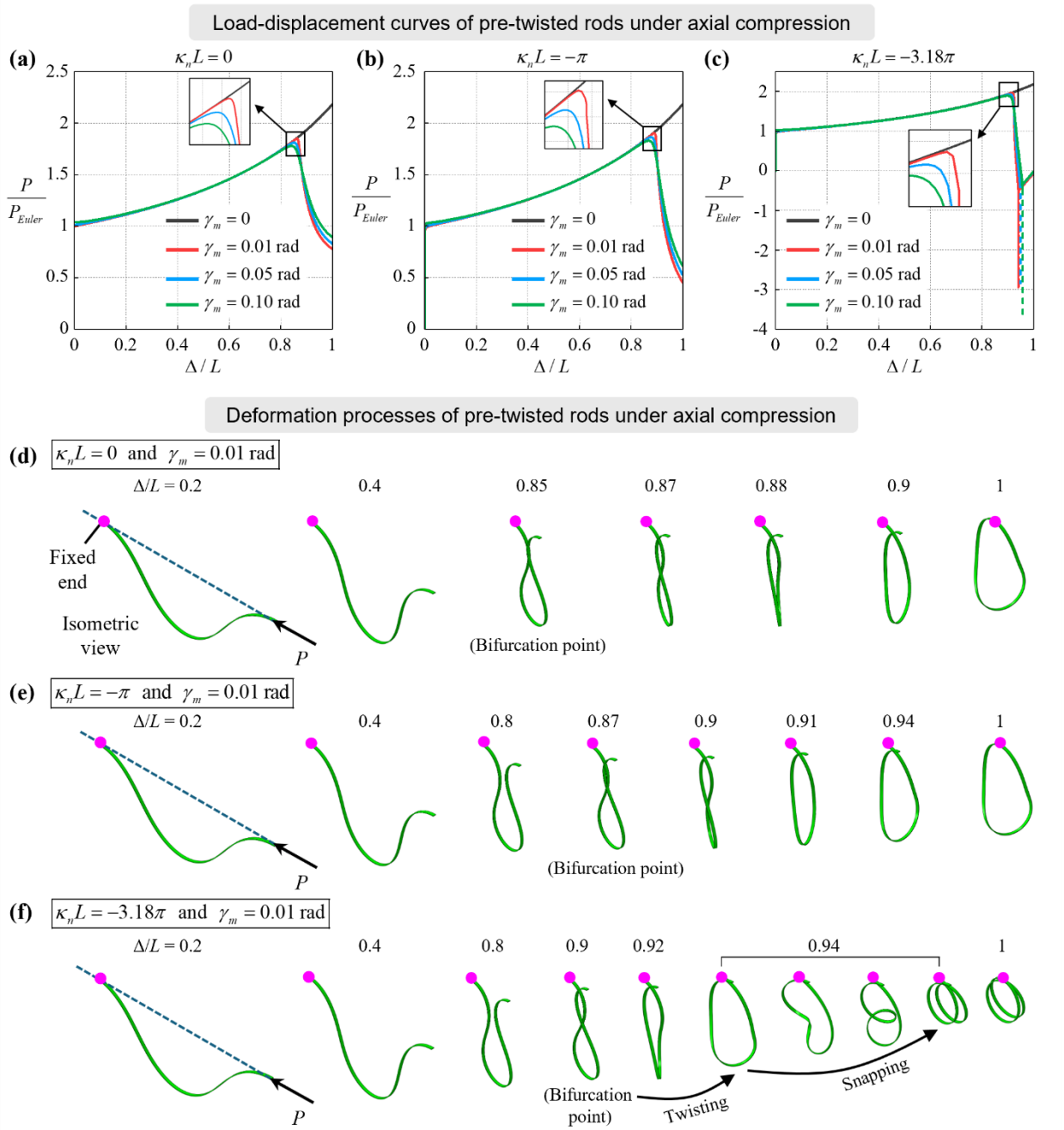

Fig. 10. Mechanical behavior of pre-twisted elastic rods with *negative* natural curvatures under axial compression, predicted by finite element simulations. (a-c) Dimensionless load P/P_{Euler} versus dimensionless end-shortening Δ/L for different pre-twisted angles γ_m: (a) $\kappa_n L = 0$; (b) $\kappa_n L = -\pi$; (c) $\kappa_n L = -3.18\pi$. Here, $P_{Euler} = 7.6231$ N is the Euler buckling load predicted by finite element simulations, which is slightly smaller than the theoretical value 7.8271 N. The dashed lines in (c) correspond to the snapping process. (d-e) Deformation processes of elastic rods with $\gamma_m = 0.01$ rad: (d) $\kappa_n L = 0$; (e) $\kappa_n L = -\pi$; (f) $\kappa_n L = -3.18\pi$. In all cases, $h/t = 4$ and $\nu = 1/3$. The dot represents the fixed end.

6. Conclusions

In this paper, we investigated the secondary out-of-plane bifurcation from the Euler buckling in clamped-clamped elastic rods with natural curvature under axial compression. The bifurcation analysis was performed based on Kirchhoff's three-dimensional theory of inextensional rods, and the critical end-shortening, critical load, and associated eigenmode at the onset of out-of-plane bifurcation were determined. Natural curvature plays a critical role in the out-of-plane bifurcation, while its effect depends significantly on the bending direction of the in-plane Euler buckling. When the Euler buckling direction is consistent with the rod's naturally curved direction, the critical end-shortening for out-of-plane bifurcation decreases as the natural curvature increases, and vice versa. As a result, by appropriately selecting the Euler buckling direction and the magnitude of natural curvature, the out-of-plane bifurcation can occur at relatively small end-shortenings without self-contact. Experiments were conducted to validate these results, and reasonable agreement was observed.

In addition, the effects of symmetric in-plane geometric imperfections and antisymmetric pre-twist geometric imperfections on the out-of-plane bifurcation were examined. Both types of geometric imperfection only produce modest changes in the critical end-shortening or critical load at bifurcation. The primary role of the in-plane imperfection is to select the Euler buckling direction, which in turn has a major effect in the presence of substantial natural curvature. By contrast, the primary role of pre-twist geometric imperfection is to trigger the out-of-plane bifurcation, which leads to post-bifurcation behavior characterized by twisting, snapping, or twisting followed by snapping, depending on the magnitude of the natural curvature and the Euler buckling direction. The rich instability behavior of Euler's elastica with natural curvature provides a new building block for reconfigurable mechanical systems that harness mechanical instability, with potential functional applications in areas such as reconfigurable mechanical metamaterials and soft robotics.

Acknowledgements

L.L., S.L., and R.R.Z. acknowledge funding support from the National Science Foundation Award CPS-2201344 and National Science Foundation Career Award CMMI-2145601.

Appendix A. Experiments

The experimental rods were all printed in their naturally curved states using polylactic acid (PLA Basic, Bambu Lab) with an X1 Carbon 3D printer. The length, cross-sectional height, and thickness were $L = 200$ mm, $h = 2.2$ mm, and $t = 0.55$ mm, respectively. As illustrated in Fig. 1(a), the naturally curved rod was first straightened and then clamped into a universal testing machine (3344, Instron, Inc., USA). The bottom end was fully fixed, while the top end was fixed but allowed to translate along the longitudinal direction for compressive displacement. The rod was axially compressed at a rate of 4 mm/s. As mentioned previously, for rods with dimensionless natural curvature $\kappa_n L = 0$, 10, and 20, listed in Table 1, out-of-plane bifurcation occurs at very large end-shortening, where self-contact takes place. Therefore, in these tests, an out-of-plane offset of h was prescribed at the top end relative to the bottom end to facilitate the onset of bifurcation.

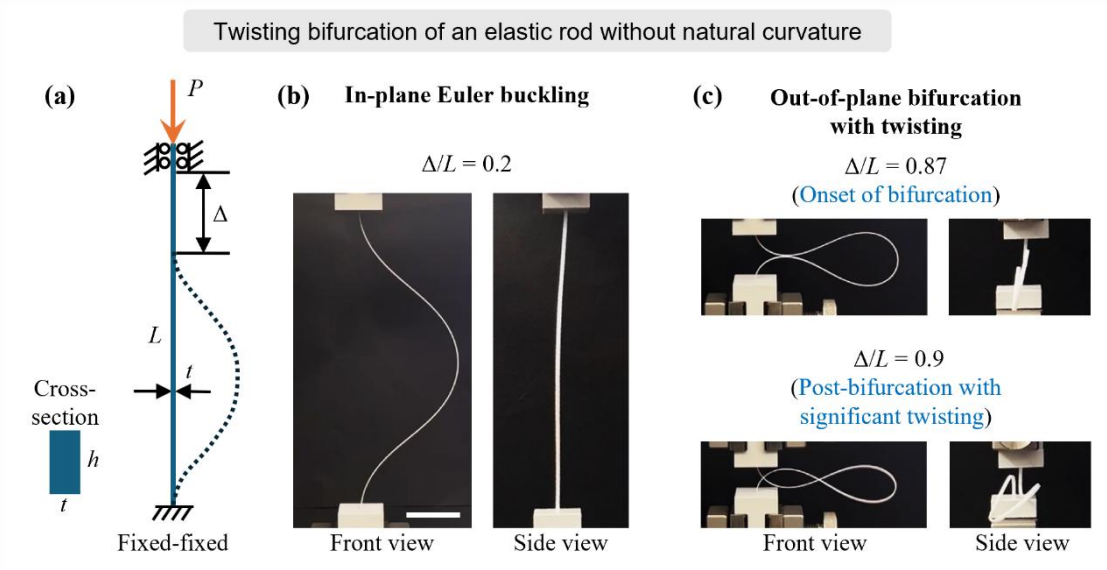

Fig. A1. Twisting bifurcation of an elastic rod without natural curvature under axial compression. (a) Schematic of an elastic rod with length L, rectangular cross-section height h, and thickness t. The rod is fixed at both ends, with the top end allowed to displace axially. In the experiment, an end-shortening Δ is prescribed, and the reaction force P is measured. (b, c) Experimental images of an elastic rod with $h/t = 4$ under axial compression. (b) At a small end-shortening, e.g., $\Delta/L = 0.2$, the rod exhibits in-plane Euler buckling. (c) As Δ/L reaches a critical value of 0.87, out-of-plane twisting bifurcation occurs, leading to significant twisting under further loading, as illustrated by the configuration at $\Delta/L = 0.9$. As mentioned earlier, to avoid self-contact and facilitate the onset of bifurcation, an out-of-plane offset is applied at the top end relative to the bottom end. Scale bar: 3 cm.

Appendix B. Finite element simulations

The mechanical behavior of elastic rods with natural curvature and pre-twist geometric imperfections under axial compression is simulated using the commercial software ABAQUS 2024 (Dassault Systèmes, France). In all simulations, C3D8R elements (8-node linear brick elements with reduced integration) are used, and self-contact and penetration are allowed. To incorporate the effect of natural curvature, the rod is modeled as a thermally stressed bilayer with orthotropic thermal expansion. The coefficients of thermal expansion (CTEs) of the two layers along the rod longitudinal direction are assumed to be equal in magnitude but opposite in sign, namely α_{T} and $-\alpha_{\mathrm{T}}$, while those in the other two directions are set to zero. A linear elastic, isotropic constitutive relation is adopted, with Young's modulus and Poisson's ratio taken as E = 2.6 GPa and v = 1/3, respectively. Consistent with the experimental rods, the length, cross-sectional height, and thickness are taken as L = 200 mm, h = 2.2 mm, and t = 0.55 mm, respectively.

Moreover, the pre-twist geometric imperfection is introduced by first applying a pair of twisting angles, $-\gamma_{\mathrm{m}}$ and γ_{m}, about the longitudinal direction of the bilayer, and then exporting the resulting deformed configuration to release the strain. The obtained stress-free pre-twisted bilayer configuration is used as the initial configuration of the rod. The two layers are assigned the same temperature change $\Delta T = t\kappa_{\mathrm{n}} / (3\alpha_{\mathrm{T}})$ [25], and α_{T} is taken as 0.002 K^{-1}. Both ends are fixed, while the loading end is allowed to translate along the axial loading direction. A static displacement-controlled loading method is used in the simulation, and a small damping factor of 10^{-8} is introduced to stabilize the simulation.

References

[1] L. Euler, Methodus inveniendi lineas curvas maximi minimive proprietate gaudentes sive solutio problematis isoperimetrici latissimo sensu accepti, 1744.

[2] L. Lu, S. Leanza, R.R. Zhao, Mechanical instabilities: from failure mechanism to functionality, Applied Mechanics Reviews, 78 (2026) 030801.

[3] L. Wang, D. Zheng, P. Harker, A.B. Patel, C.F. Guo, X. Zhao, Evolutionary design of magnetic soft continuum robots, Proceedings of the National Academy of Sciences, 118 (2021) e2021922118.

[4] Y. Kim, G.A. Parada, S. Liu, X. Zhao, Ferromagnetic soft continuum robots, Science Robotics, 4 (2019) eaax7329.
[5] X. Bao, F. Wang, J. Zhang, M. Li, S. Zhang, Z. Ren, J. Liao, Y. Yan, W. Kang, R. Zhang, Real-time in situ magnetization reprogramming for soft robotics, Nature, 645 (2025) 375-384.
[6] F. Zhang, S. Li, Z. Shen, X. Cheng, Z. Xue, H. Zhang, H. Song, K. Bai, D. Yan, H. Wang, Rapidly deployable and morphable 3D mesostructures with applications in multimodal biomedical devices, Proceedings of the National Academy of Sciences, 118 (2021) e2026414118.
[7] Z. Fan, Y. Yang, F. Zhang, Z. Xu, H. Zhao, T. Wang, H. Song, Y. Huang, J.A. Rogers, Y. Zhang, Inverse design strategies for 3D surfaces formed by mechanically guided assembly, Advanced Materials, 32 (2020) 1908424.
[8] K. Bertoldi, V. Vitelli, J. Christensen, M. Van Hecke, Flexible mechanical metamaterials, Nature Reviews Materials, 2 (2017) 1-11.
[9] B. Florijn, C. Coulais, M. van Hecke, Programmable mechanical metamaterials, Physical Review Letters, 113 (2014) 175503.
[10] A. Goriely, R. Vandiver, M. Destrade, Nonlinear euler buckling, Proceedings of the royal society A: mathematical, physical and engineering sciences, 464 (2008) 3003-3019.
[11] Y. Chen, L. Jin, From continuous to snapping-back buckling: A post-buckling analysis for hyperelastic columns under axial compression, International Journal of Non-Linear Mechanics, 125 (2020) 103532.
[12] S. Zhao, P.A. Haas, Euler buckling on curved surfaces, Physical Review Letters, 135 (2025) 247201.
[13] B. Radisson, E. Kanso, Elastic snap-through instabilities are governed by geometric symmetries, Physical Review Letters, 130 (2023) 236102.
[14] Q. Wang, A. Giudici, W. Huang, Y. Wang, M. Liu, S. Tawfick, D. Vella, Transient amplification of broken symmetry in elastic snap-through, Physical Review Letters, 132 (2024) 267201.
[15] K. Chen, W. Zhong, Z. Yu, C. Bruce, Y.P. Korkolis, Asymmetric buckling and mode-switching, of an elastica under a lateral restraining force, International Journal of Non-Linear Mechanics, (2026) 105346.
[16] Y. Zhang, W. Huang, M. Liu, J. Yu, H. Gao, Achieving symmetric snap-through buckling via designed magnetic actuation, Science Advances, 11 (2025) eadw1259.

[17] S. Leanza, R.R. Zhao, J.W. Hutchinson, On the elastic stability of folded rings in circular and straight states, European Journal of Mechanics-A/Solids, 104 (2024) 105041.
[18] S. Leanza, R.R. Zhao, J.W. Hutchinson, The elastica with pre-stress due to natural curvature, Journal of the Mechanics and Physics of Solids, 190 (2024) 105690.
[19] S. Leanza, J. Lee, L. Lu, R.R. Zhao, Elastic rod origami (RodOri) for programming static and dynamic mechanical properties, Science Advances, 12 (2026) eaed1774.
[20] J. Maddocks, Stability of nonlinearly elastic rods, Archive for Rational Mechanics and Analysis, 85 (1984) 311-354.
[21] Y. Miyazaki, K. Kondo, Analytical solution of spatial elastica and its application to kinking problem, International Journal of Solids and Structures, 34 (1997) 3619-3636.
[22] D. Stump, G. Van Der Heijden, Birdcaging and the collapse of rods and cables in fixed-grip compression, International Journal of Solids and Structures, 38 (2001) 4265-4278.
[23] G. Van der Heijden, S. Neukirch, V. Goss, J. Thompson, Instability and self-contact phenomena in the writhing of clamped rods, International Journal of Mechanical Sciences, 45 (2003) 161-196.
[24] I.S. Sokolnikoff, Mathematical theory of elasticity, McGraw-Hill New York, 1956.
[25] L. Lu, J. Dai, S. Leanza, J.W. Hutchinson, R.R. Zhao, Multiple equilibrium states of a curved-sided hexagram: Part II—Transitions between states, Journal of the Mechanics and Physics of Solids, 180 (2023) 105407.